


 Cite this: *RSC Adv.*, 2024, 14, 34051

# Enhancing perovskite solar cell performance through $\text{PbI}_2$ *in situ* passivation using a one-step process: experimental insights and simulations†

 Selma Rabhi,<sup>a</sup> Karthick Sekar,<sup>b</sup> Karol Kalna,<sup>c</sup> Tarak Hidouri,<sup>d</sup> Dip Prakash Samajdar,<sup>e</sup> Babban Kumar Ravidas,<sup>f</sup> Hichem Bencherif,<sup>g</sup> Roberto Fornari,<sup>dh</sup> Kouloud Albaidani<sup>i</sup> and M. Khalid Hossain<sup>j</sup>

The *in situ* passivation of a methylammonium lead triiodide ( $\text{MAPbI}_3$ ) phase spin-coated *via* a one-step process was experimentally investigated to elucidate their fundamental properties. Structural analysis revealed that  $\text{MAPbI}_3$  adopts a tetragonal crystal structure with a small excess of  $\text{PbI}_2$  (0.03 M) segregating at grain boundaries. Optical characterization indicated a band gap of 1.53 eV, highlighting the material's potential as an effective visible light absorber. To facilitate the fabrication of efficient perovskite solar cells (PSCs), we employed a primary n-i-p planar structure ( $\text{ITO}/\text{SnO}_2/\text{MAPbI}_3/\text{spiro-OMeTAD}/\text{Au}$ ) in drift-diffusion SCAPS-1D simulations using experimental data from  $\text{MAPbI}_3$  layers containing excess  $\text{PbI}_2$ . The simulations predicted a high power conversion efficiency (PCE) of approximately 24%. We further analyzed the impact of series resistance, shunt resistance,  $\text{MAPbI}_3$  thickness, defect density, as well as radiative and Auger recombination on photovoltaic performance, aiming to identify optimal parameters for enhanced device efficiency. Additionally, the use of ohmic contacts with AZO and IZO as the front and rear contacts, respectively, in the optimized device structure ( $\text{AZO}/\text{SnO}_2/\text{MAPbI}_3/\text{spiro-OMeTAD}/\text{IZO}$ ) resulted in a PCE of 26.03%. These findings provide valuable insights for future research aimed at achieving high-efficiency bifacial  $\text{MAPbI}_3$  perovskite solar cells.

 Received 27th August 2024  
 Accepted 12th October 2024

DOI: 10.1039/d4ra06193d

[rsc.li/rsc-advances](https://rsc.li/rsc-advances)

<sup>a</sup>Laboratory of Innovative Environmental Preservation Techniques, Department of Chemistry, Constantine 1 University, 25000 Constantine, Algeria. E-mail: selma.rabhi@umc.edu.dz

<sup>b</sup>IM2NP, CNRS UMR 7334, Aix-Marseille University, 13397 Marseille, France

<sup>c</sup>Nanoelectronics Devices Computational Group, Department of Electronic & Electrical Engineering, Faculty of Science & Engineering, Swansea University, Swansea, SA1 8EN, UK

<sup>d</sup>Department of Mathematical, Physical and Computer Sciences, University of Parma, 43124, Parma, Italy. E-mail: tarek.hidouri@unipr.it

<sup>e</sup>Department of ECE, Indian Institute of Information Technology, Design & Manufacturing, Jabalpur, Madhya Pradesh 482005, India

<sup>f</sup>Department of Natural Science, Indian Institute of Information Technology, Design & Manufacturing, Jabalpur, Madhya Pradesh, 482005, India

<sup>g</sup>LEREESI, Higher National School of Renewable Energies, Environment and Sustainable Development, Batna 05078, Algeria

<sup>h</sup>MEM-CNR, Institute of Materials for Electronics and Magnetism, 43124, Parma, Italy

<sup>i</sup>Physics Department, Faculty of Science, King Khalid University, Abha 61411, Saudi Arabia

<sup>j</sup>Institute of Electronics, Atomic Energy Research Establishment, Bangladesh Atomic Energy Commission, Dhaka 1349, Bangladesh

† Electronic supplementary information (ESI) available: Material description, instrumentation, experimental synthetic procedures of the  $\text{MAPbI}_3$  film including strutting precursors and filtration. Additional analyses including a comparison between the bandgap determination performed according to the approach outlined by Tauc and a new approach based on linear fit employed as an abscissa for the slope below the fundamental absorption. See DOI: <https://doi.org/10.1039/d4ra06193d>

## 1. Introduction

The development of affordable, efficient, and stable solar technology has progressed rapidly in recent years to accelerate the world's energy transition. 3D hybrid PSCs have dominated the best cell efficiencies in emerging photovoltaic technology.<sup>1,2</sup> Unveiling the full potential of 3D hybrid perovskites remains a key research focus. Despite the remarkable achievements of 3D hybrid perovskites, scientists are relentlessly pursuing innovative methods to optimize their performance. Moreover, the introduction of a novel synthesis technique aimed at controlling crystallization has significantly enhanced the PCE of PSCs, achieving a ground-breaking efficiency of 26.1%.<sup>3</sup> This milestone matches the previous record set by Korean researchers, who also attained this PCE by successfully controlling crystallization.<sup>4</sup> 3D hybrid PSCs have achieved these high performances because of their attractive physical properties, such as high absorption coefficient, tuneable band gap *via* halide substitution, easy photo-generation of free charges, long carrier diffusion length, low trap density, low non-radiative recombination rate,<sup>5</sup> and good mechanical properties, which make them suitable for flexible solar cells.<sup>6,7</sup> Additionally, a simple synthesis process at low temperatures (150–200 °C of thermal annealing) is suitable for a low-cost fabrication.<sup>8–10</sup> Despite all these advantages and higher PCE, 3D PSCs still



suffer from stability issues due to their morphology. The perovskite thin layer is mostly polycrystalline and comprises many small crystalline grains with numerous grain boundaries (GBs).<sup>11</sup> However, GBs attract moisture and oxygen.<sup>12,13</sup> These defects disrupt the ordered crystalline structure and can act as recombination for photo-generated charge carriers, providing pathways for electrons and holes to recombine before being extracted from the device.<sup>14</sup>

Moreover, the presence of impurities in GBs introduces electronic trap states within the band gap of the perovskite layer. These trap states can hinder charge carriers from reaching device contacts,<sup>15</sup> leading to the reduced performance and stability of PSCs.<sup>16,17</sup> Several approaches have been developed to reduce the density of defects and traps.<sup>18–20</sup> The control of the crystallization process and film morphology can potentially minimize these defects, thereby improving efficiency and stability.<sup>21</sup> This control is achieved through incorporation of a small excess of  $\text{PbI}_2$ , which serves as an effective route for passivation.<sup>22</sup> The excess  $\text{PbI}_2$  preferentially segregates to grain boundaries and surfaces, resulting in the passivation of the 3D perovskite layer by suppressing interfacial recombination and reducing ionic defects, which leads to the improvement of performance.<sup>23</sup> Hence, the 3D perovskite structure is formed on three different components with a general formula  $\text{ABX}_3$ ,<sup>24</sup> where A is an organic/inorganic cation, such as formamidinium iodide (FAI), methylammonium iodide (MAI), or cesium (Cs); B is a metal cation (typically  $\text{Pb}^{2+}$ ); and X is a halide anion (*i.e.*,  $\text{Cl}^-$ ,  $\text{Br}^-$ ,  $\text{I}^-$ ).  $\text{MAPbI}_3$  is predominantly favored for use in PSCs due to its easier synthesis compared to  $\text{FAPbI}_3$ . The majority of PSCs are prepared using wet synthesis methods,<sup>25,26</sup> which offer two approaches: one-step and two-step methods.<sup>27</sup> However, the one-step method is more commonly employed due to its

simplicity and practicality in device fabrication. This study examines the  $\text{PbI}_2$  *in situ* passivation on the  $\text{MAPbI}_3$  perovskite films at room temperature and under ambient conditions. Passivation is performed during the process of deposition of  $\text{MAPbI}_3$  thin layer by applying the one-step method, which involves spin-coating at different speeds. Moreover, we proceed experimentally to analyse the  $\text{MAPbI}_3$  physical properties to achieve the optimal solar cell design. These physical properties are used in simulations using a Solar Cell Capacitance Simulator SCAPS-1D version 3.3.10.<sup>28–32</sup> In this study, based on the experimental results of our samples used to extract the photovoltaic parameters of the PSC device, we initially design and then simulate a one-dimensional planar PSC of n-i-p type ITO/ $\text{SnO}_2$ / $\text{MAPbI}_3$ /spiro-OMeTAD/Au.

Fig. 1(b) depicts the energy band diagram of the simulated device. The efficiency of charge transfer, which is vital for the performance of solar cells, depends on the meticulous alignment of energy levels between the perovskite absorber and the interface layers.<sup>33</sup> The Electron Transport Layer (ETL) must have a Conduction Band (CB) level that is lower than that of the perovskite (PVK). This difference in the CB, known as the Conduction Band Offset (CBO), facilitates the easy transfer of photo-generated electrons from the PVK to the ETL, and simultaneously, the Fermi level of the ETL must align with or be slightly lower than the Fermi level of the PVK to ensure smooth electron flow without creating an energy barrier. This is because the electrons are thermodynamically inclined to move towards the ETL's lower energy levels.<sup>34</sup> Conversely, the Valence Band (VB) of the HTL should be higher than that of the PVK, with the Fermi levels of the HTL and PVK aligned to promote effective hole transfer. This Valence Band Offset (VBO) enables the effective extraction of holes from the PVK into the HTL, as the

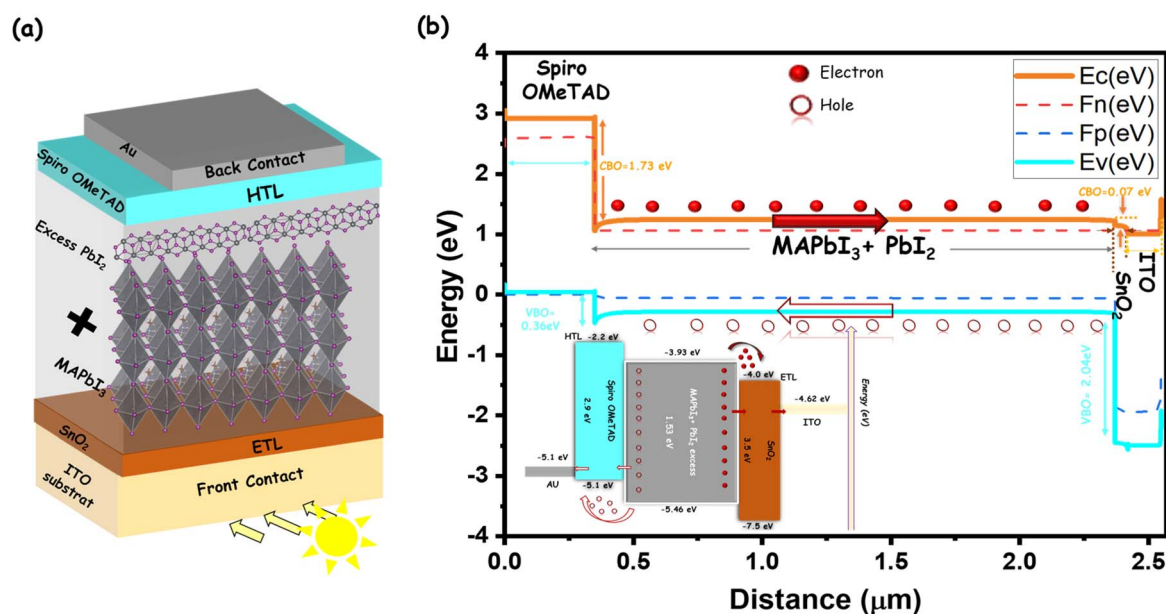


Fig. 1 (a) Schematic of a n-i-p structure for the PSC used in SCAPS simulations: ITO/ $\text{SnO}_2$ / $\text{MAPbI}_3$ /spiro-OMeTAD/Au; (b) energy band diagram for the device. Inset: an energy level diagram of different materials used in the PSC with the values of BC and BV of the ETL and HTL of the selected materials.



holes are driven towards the higher energy vacant states in the HTL's VB. The CBO at SnO<sub>2</sub>/PVK is lower (−0.07 eV), and an energy cliff is formed at the SnO<sub>2</sub>/PVK interface. This modest energy cliff does not hinder electron movement toward the ETL. In other words, no barrier is formed, allowing electrons to flow effortlessly from the absorber to the ETL due to their natural tendency to move towards lower energy states.<sup>34,35</sup> Electrons tend to be transferred from MAPbI<sub>3</sub> to SnO<sub>2</sub> and then to the ITO layer to be collected, while holes are repulsed from this side. However, the VBO at the PVK/spiro-OMeTAD interface exhibits a positive value (0.36 eV). In this case, a spike is formed at this interface, which acts as a barrier to electrons. Due to this energy barrier created by the positive VBO, holes tend to migrate from the lower energy PVK layer to the higher energy HTL layer, facilitating efficient hole injection and transport.<sup>36</sup> Additionally, both electrodes should facilitate better charge transfer from adjacent layers, and their work functions should match the energy levels of adjacent layers.<sup>35,37,38</sup> This strategic engineering of energy level alignments guarantees a selective extraction and transport of charge carriers and, ultimately, increases the collection of loads and, therefore, the performance of solar cells.<sup>39</sup>

## 2. Experimental and numerical simulation section

### 2.1 Experimental section about MAPbI<sub>3</sub> film synthesis

The *in situ* passivation is achieved using directly a small excess of PbI<sub>2</sub> in the primary MAPbI<sub>3</sub> precursor solution by a mixing ratio of 1 : 0.03 M of the initial MAI : PbI<sub>2</sub> within 2.873 ml *N,N*-dimethyl formamide (DMF) under atmosphere conditions, and annealing at 100 °C for a short time was required for the crystallization of MAPbI<sub>3</sub>. This method promotes *in situ* passivation without the need for additional post-deposition PbI<sub>2</sub> treatments, as the excess PbI<sub>2</sub> segregates to the grain boundaries and surfaces, passivating defects directly during the film formation. Grazing incidence X-ray diffraction (GIXRD) measurements were carried out using a Philips X' Pert diffractometer with Cu K $\alpha$  radiation ( $\lambda = 1.5418 \text{ \AA}$ ) for an *ex situ* measurement of this sample from 10° to 60° at room temperature. UV-visible absorption spectra were recorded using a Shimadzu UV-3101PC UV-vis-NIR spectrophotometer. A profilometer ALTI-SURF 500 was used to measure the thickness of the layer deposited on the substrate. However, Fig. S1† summarizes the synthesis process of MAPbI<sub>3</sub> and PbI<sub>2</sub> segregation on it.

### 2.2 Numerical section

Solar Cell Capacitance Simulator SCAPS-1D allows us to study the influence of perovskite and other solar cell layer thicknesses under different conditions (ideal and non-ideal) on photovoltaic parameters. Moreover, it permits us to investigate the device performance with respect to several input parameters, such as relative permittivity, band gap, and bulk charge carrier density of ETL, HTL, and parasitic resistances. The simulation here is based on a classical drift-diffusion model, which solves

the electron (1) and hole (2) continuity equations and Poisson's eqn (3):

$$\frac{\partial}{\partial x} \left( -\varepsilon(x) \frac{\partial V}{\partial x} \right) = q[p(x) - n(x) + N_D^+(x) - N_A^-(x) + p_t(x) - n_t(x)], \quad (1)$$

$$\frac{\partial n}{\partial t} = \frac{1}{q} \frac{\partial J_n}{\partial x} + G_n - R_n, \quad (2)$$

$$\frac{\partial p}{\partial t} = -\frac{1}{q} \frac{\partial J_p}{\partial x} + G_p - R_p, \quad (3)$$

where  $\varepsilon$ ,  $V$ ,  $q$ ,  $p(x)$ ,  $n(x)$ ,  $N_D^+(x)$ ,  $N_A^-(x)$ ,  $p_t(x)$ , and  $n_t(x)$  are the dielectric permittivity, electric potential, electronic charge, free hole density, free electron density, donor density, acceptor density, trap density of holes, and trap density of electrons, respectively.

The simulations conducted are used as input experimental optical characteristics, such as the band gap and the thickness of the MAPbI<sub>3</sub> absorber. A systematic investigation and optimization of the absorber thickness, defect density, series resistance ( $R_S$ ), shunt resistance ( $R_{Sh}$ ), radiative recombination coefficient, Auger electron capture coefficient, interfacial defects densities, and the impact of the front and rear contact on the overall performance of the PSC device are conducted. The simulations are carried out at 300 K under one sun irradiation with an integrated power density of 1000 W m<sup>−2</sup> (AM 1.5 G 1000 W cm<sup>−2</sup>). This irradiation is chosen according to standard solar cell test conditions.<sup>44</sup> The optical band gap of the absorber layers (MAPbI<sub>3</sub>) and their thickness is obtained from experimental transmittance and UV measurements. Other parameters of the active layer, HTL, and ETL, such as thicknesses, band gap, electron affinity, permittivity, the effective density of states, charge mobility, thermal velocity, doping density, and defect density, are extracted from the literature.<sup>41–43,45</sup> The ETL and HTL absorption curves are generated by SCAPS software, which are calculated using eqn (3), where  $A_\alpha = 10^5$ . All the input parameters used in the simulations are listed in Table 1.

## 3. Results and discussion

### 3.1 Structural and optical properties

GIXRD is particularly beneficial for analyzing thin films because it is sensitive to surface layers and detects crystal planes parallel to the substrate. In Fig. 2, the GIXRD pattern of excess PbI<sub>2</sub> MAPbI<sub>3</sub> film is compared to pristine MAPbI<sub>3</sub> film, as reported by Belaidi *et al.*<sup>40</sup> The structural behavior of the excess PbI<sub>2</sub> film closely resembles that of the pristine perovskite film, showing intense diffraction peaks at 14.00° and 28.27°, corresponding to the (110) and (220) crystal planes of the tetragonal perovskite structure,<sup>46</sup> with lattice parameters  $a = 8.912 \text{ \AA}$  and  $c = 12.604 \text{ \AA}$ .<sup>47</sup> Peaks at 12.60°, 37.83°, and 52.32°, attributed to the (001), (003), and (004) planes, respectively, indicate the presence of excess PbI<sub>2</sub>.<sup>48</sup> The reduced intensity of the PbI<sub>2</sub> peaks in GIXRD measurements may result from the geometry of the technique, which primarily detects planes parallel to the substrate, potentially omitting PbI<sub>2</sub> crystals with varying orientations. This



Table 1 Simulation input parameters of the perovskite solar cells<sup>a</sup>

Parameters	ITO	SnO <sub>2</sub>	MAPbI <sub>3</sub>	Spiro-OMeTAD
Thickness <i>e</i> (μm)	0.130	0.05	2.02*	0.350
Bandgap <i>E<sub>g</sub></i> (eV)	3.6	3.5	1.53*	2.9
Electron affinity $\chi$ (eV)	4.0	4	3.93	2.2
Dielectric permittivity $\epsilon$ (relative)	10	9	6.5	3
CB effective density of states (cm <sup>-3</sup> )	$2.2 \times 10^{18}$	$2.2 \times 10^{18}$	$2.2 \times 10^{18}$	$2.2 \times 10^{18}$
VB effective density of states (cm <sup>-3</sup> )	$1.8 \times 10^{19}$	$1.8 \times 10^{19}$	$1.3 \times 10^{19}$	$2.2 \times 10^{18}$
Electron mobility $\mu_e$ (cm <sup>2</sup> V <sup>-1</sup> s <sup>-1</sup> )	1.0	1.0	2	$1.0 \times 10^{-4}$
Hole mobility $\mu_h$ (cm <sup>2</sup> V <sup>-1</sup> s <sup>-1</sup> )	2.5	2.0	2	$1.0 \times 10^{-4}$
Shallow uniform acceptor density, $N_A$ (cm <sup>-3</sup> )	0	0	$1 \times 10^{19}$	$1.0 \times 10^{20}$
Shallow uniform donor density $N_D$ (cm <sup>-3</sup> )	$2 \times 10^{19}$	$2 \times 10^{17}$	$1 \times 10^{19}$	0
Defect density (cm <sup>-3</sup> )	—	$1 \times 10^{15a}$	$1 \times 10^{15a}$	$1 \times 10^{15a}$
References	41	42	36 and 43	43

<sup>a</sup> (\*) indicates the experimental value in this current work. (a) In this study, these values remain constant during initial optimization to obtain the best combination of HTL, ETL, and absorber.

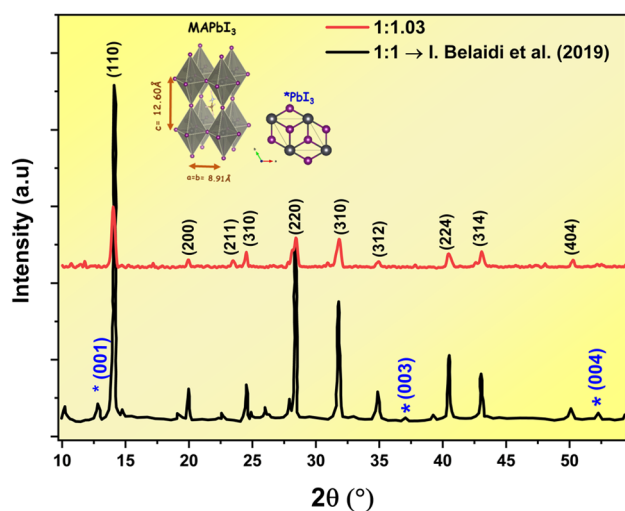


Fig. 2 GIXRD pattern of the excess PbI<sub>2</sub> MAPbI<sub>3</sub> film compared to the pristine MAPbI<sub>3</sub> film.<sup>40</sup>

could be explained by the interaction of the MAPbI<sub>3</sub> precursors (MAI and PbI<sub>2</sub>) during annealing, where the octahedral PbI<sub>6</sub> units arrange themselves into a 3D tetragonal structure, with MA<sup>+</sup> ions occupying the center of the framework, surrounded by eight octahedral PbI<sub>6</sub> units, resulting in MAPbI<sub>3</sub> adopting a tetragonal crystal structure at room temperature. Furthermore, the excess PbI<sub>2</sub> in the MAPbI<sub>3</sub> precursor solution remains unreacted and organizes itself into a 2D hexagonal lattice.<sup>49,50</sup> Because the crystal structures of PbI<sub>2</sub> and MAPbI<sub>3</sub> differ significantly, direct epitaxial growth of perovskite on the PbI<sub>2</sub> (001) plane is unlikely. However, one possible explanation for the locally oriented growth of perovskite crystals could be 'pseudo-epitaxial' nucleation, as reported by Brenner *et al.*<sup>51</sup> In this scenario, the tetragonal perovskite (202) plane, which closely resembles the PbI<sub>2</sub> (001) plane in bonding and lattice parameters, may serve as the nucleation site. With this alignment, subsequent crystal growth occurs at an approximate 45° angle along the perovskite (002) plane, allowing the structure to accommodate the differing lattice parameters of PbI<sub>2</sub> and

MAPbI<sub>3</sub>. This segregation pattern can be rationalized by noting that if PbI<sub>2</sub> was located within the perovskite grains instead of at the grain boundaries, it induces a change in the lattice parameters. However, the literature findings commonly report the lattice parameters of MAPbI<sub>3</sub> as  $a = 8.912 \text{ \AA}$  and  $c = 12.604 \text{ \AA}$ .<sup>52,53</sup> This observation supports the conclusion that PbI<sub>2</sub> segregation predominantly occurs at the grain boundaries rather than within the perovskite grains. Consequently, the observed passivation effect may arise from band bending at the interface between the perovskite and PbI<sub>2</sub>, as suggested in the work by Chen *et al.*<sup>54</sup> The obtained results show crystallites with an average size of 179.8 nm. These grain sizes are in the range observed in high-performance MAPbI<sub>3</sub> solar cells, which should be greater than 100 nm.<sup>11</sup> This means that the spin conditions chosen for depositing MAPbI<sub>3</sub> are suitable for obtaining a high-quality MAPbI<sub>3</sub> layer.

Furthermore, the recent report of Zhang *et al.* findings<sup>55</sup> also confirmed that the slightly excess PbI<sub>2</sub> (1.05 M) perovskite film, which is marginally closer to our chosen excess PbI<sub>2</sub> (1.03 M) perovskite composition, demonstrates a similar tendency to our results. Interestingly, their results also demonstrated that the excess PbI<sub>2</sub> (1.05 M) perovskite device displayed an enhanced power conversion efficiency (16.5%) compared to the pristine solar cell (14.3%). In general, the excessive PbI<sub>2</sub> introduces extra I-into the MAPbI<sub>3</sub> perovskite, which significantly alters the halide vacancies and reduces the defect-induced nonradiative recombination.<sup>55,56</sup>

To investigate the thickness of the sample, a Profilometer ALTISURF 500 was used. The measured thickness is above  $2.02 \pm 0.005 \text{ \mu m}$ , and this thickness is used in the next part. The absorption spectrum is shown in Fig. 3(a). The absorption spectrum of the MAPbI<sub>3</sub> film on glass, measured from 300 nm to 860 nm, demonstrates a broad absorption range that encompasses both visible and near-infrared wavelengths. Notably, there is an increase in absorption at shorter wavelengths (around 810 nm), with an absorption coefficient ( $\alpha$ ) of approximately  $5 \times 10^3 \text{ cm}^{-1}$ . The deposited layer appears almost black (grey-dark), which indicates good absorption. This observation is consistent with the known optical properties of



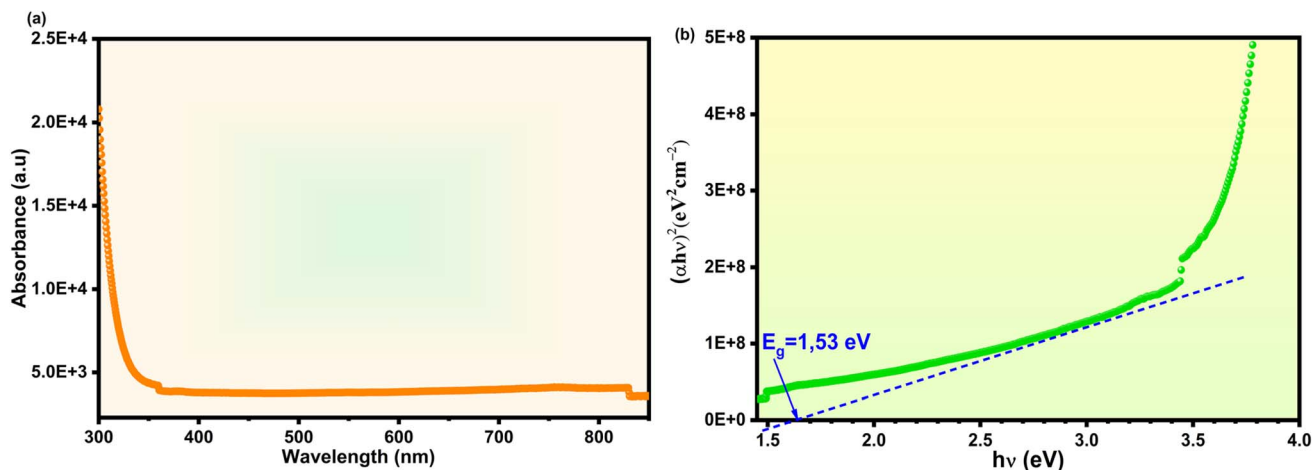


Fig. 3 (a) UV-visible absorbance spectra of MAPbI<sub>3</sub>; (b) the corresponding Tauc plot used for band gap calculations.

perovskite materials, where a darker color generally corresponds to higher light absorption due to increased optical density and effective bandgap utilization.<sup>57,58</sup> Additionally, excessive PbI<sub>2</sub> treatment is found to passivate grain boundaries and suppress the formation of trap states in the perovskite material, enhancing charge carrier movement and decreasing recombination, which enhances absorption.<sup>59</sup>

Furthermore, from the transmittance spectra (see Fig. 3(a)), and based on the Beer-Lambert law defined using eqn (4), we estimate the band gap of the film, whereas the absorption curve is calculated as follows:

$$T = e^{-\alpha d} \quad (4)$$

Moreover, the bandgap  $E_g$  was estimated using the Tauc relation as follows:

$$\alpha hv = A[hv - E_g]^n, \quad (5)$$

where  $d$  is the thickness of MAPbI<sub>3</sub> layers (2.02 μm extracted experimentally),  $A$  is a constant, and the parameter  $n$  was taken as equal to 1/2 for the direct band gap. The estimated band gap of 1.53 eV (Fig. 3(b)) is useful for simulations in the next subsection. Furthermore, Makula *et al.*<sup>60</sup> suggested a method for accurately determining the band gap energy based on UV-vis spectra. As shown in Fig. S2,<sup>†</sup> we found almost the same band gap energy using this method as we did when employing the classical method.

### 3.2 Theoretical analysis of device performance

The  $J$ - $V$  characteristics obtained from the simulations of the primary device (ITO/SnO<sub>2</sub>/MAPbI<sub>3</sub>/spiro-OMeTAD/Au) carried out using photovoltaic parameters, such as open circuit voltage ( $V_{OC}$ ), short circuit current ( $J_{SC}$ ), fill factor (FF) and PCE, are shown in Fig. 4, where  $V_{OC} = 1.00$  V,  $J_{SC} = 35.04$  mA cm<sup>-2</sup>, FF = 68.01%, and PCE = 23.93%. These promising results can be attributed to the enhancement of the perovskite/HTL interface, indicating that an excess of PbI<sub>2</sub> improves device performance

and leads to higher photovoltaic efficiency. The incorporation of a small excess of PbI<sub>2</sub> serves as an effective pathway for passivation, as reported in the literature.<sup>48,61–63</sup> When carefully managed, excess PbI<sub>2</sub> helps maintain a balance between crystallinity and the suppression of interfacial recombination, as it preferentially segregates at grain boundaries and surfaces, thereby improving performance.<sup>23</sup> Promising results can be attributed to the enhancement of.<sup>59</sup> Moreover, the performance of solar cells relies on aligning the energy levels, which are crucial for efficient charge transfer between the perovskite absorber and interface layers.<sup>33</sup> In summary, the chosen material layers in this cell exhibit suitable energy alignment conditions. Consequently, this work proposes a simple *in situ* passivation using a one-step method in the device design of ITO/SnO<sub>2</sub>/MAPbI<sub>3</sub>/spiro-OMeTAD/Au, achieving a PCE above 24%. This highlights the role of excess PbI<sub>2</sub> in enhancing PSC performance, with these photovoltaic parameters being

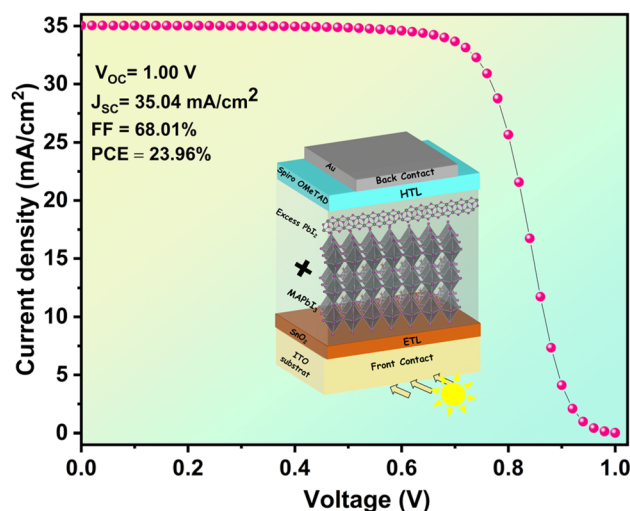


Fig. 4  $J$ - $V$  characteristics of the MAPbI<sub>3</sub>-based solar cell using the photovoltaic parameters obtained from simulation.



encouraging compared to published reports in the literature.<sup>13,48,59</sup>

**3.2.1 Impact of the series and shunt resistance on photovoltaic performances.** For high-efficiency devices, series resistance ( $R_s$ ) should not exceed  $1 \Omega \text{ cm}^2$ , and the shunt resistance ( $R_{sh}$ ) should be greater than  $10^7 \Omega \text{ cm}^2$ .<sup>64</sup>  $R_s$  originates from the impedance of electrodes, including the front and the back contacts (ITO and Au). However, the  $R_{sh}$  effect arises from manufacturing defects. Therefore, to understand the impact of parasitic resistances ( $R_s$  and  $R_{sh}$ ) on the efficiency of the PSC, which converts solar cell power into electrical energy, we incorporate them into the SCAPS-1D model. Fig. 6a–d depicts the contour mapping of the  $R_s$  and  $R_{sh}$  resistances and their effect on the PSC performance.  $R_s$  and  $R_{sh}$  are varied from 0 to  $8 \Omega \text{ cm}^2$  and 10 to  $10^8 \Omega \text{ cm}^2$ , respectively.  $R_s$  and  $R_{sh}$  regulate the  $J$ – $V$  characteristics, which have a significant effect on the device performance.  $R_s$  includes different resistances, such as the resistance due to metal contact, and resistance at the interface between layers, and each bulk layer has its resistance.  $R_{sh}$  is influenced by the device architecture. This is due to the variation in the charge recombination process, including the leakage current across cell edges.<sup>65</sup> Fig. 5a–d illustrates that all the PSC performances exhibit dropping-downs, with an increase in  $R_s$ . Fig. 5(a) shows that  $V_{OC}$  is negligible and independent from  $R_s$ . The  $J_{SC}$  of the PSC decreases slowly from 35.04 to 34.88  $\text{mA cm}^{-2}$ , as presented in Fig. 5(b), while the FF is observed to be reduced from 69.70 to 43.80%, as depicted in Fig. 5(c). Fig. 5(d) shows that PCE is reduced from 22.98% to 14.90%. An increase in  $R_s$  leads to a reduction in FF and PCE due to increased power dissipation, as initially stated above.<sup>66</sup> However, when  $R_{sh}$  is sufficiently high (above  $5 \times 10^6 \Omega \text{ cm}^2$ ), FF and PCE tend to improve. This improvement occurs because a high  $R_{sh}$  minimises leakage currents, thereby increasing the efficiency of the p–n junction and allowing more photocurrent to be collected. Although  $J_{SC}$  remains relatively constant,  $V_{OC}$  increases slowly due to reduced recombination at higher  $R_{sh}$  values, supporting better overall device performance.<sup>67</sup>

**3.2.2 Impact of the thickness and defect density ( $N_t$ ) of MAPbI<sub>3</sub> on photovoltaic performances.** The optimum conditions belong to the effect of the thickness, and the density of the defects ( $N_t$ ) in the absorbing layer plays a crucial role in light absorption and charge generation in PSCs. Contour maps of the projected  $V_{OC}$ ,  $J_{SC}$ , FF, and PCE with varying absorber thickness (1  $\mu\text{m}$  to 3  $\mu\text{m}$ ) and  $N_t$  ( $1 \times 10^{10} \text{ cm}^{-3}$  to  $1 \times 10^{16} \text{ cm}^{-3}$ ) for the MAPbI<sub>3</sub>-based PSCs are extracted, as shown in Fig. 5(a')–(d'). These contour maps illustrate how the photovoltaic parameters are affected by the combined change in the absorber  $N_t$  and the thickness. In Fig. 5(a'), the  $V_{OC}$  remains relatively constant once the thickness increases and  $N_t$  is lower than  $1 \times 10^{14} \text{ cm}^{-3}$ . As  $N_t$  is increased to values higher than  $1 \times 10^{14} \text{ cm}^{-3}$ ,  $V_{OC}$  decreases slightly from 0.990 V to 0.596 V. This means that the defect's density is mainly responsible for the observed change in  $V_{OC}$  for the conventionally structured solar cell.<sup>68</sup>

Simultaneously, Fig. 5(b') shows that the  $J_{SC}$  extended to a maximum of 44.7  $\text{mA cm}^{-2}$  when the  $N_t$  was higher than  $5 \times 10^{14} \text{ cm}^{-3}$  and an absorber thickness was higher than 3  $\mu\text{m}$ . Meanwhile, the  $J_{SC}$  increases steadily with thickness. This can

be explained by the heightened light absorption in the thicker absorber layer, leading to enhanced current generation.<sup>43</sup> However, an inversely proportional relationship between increasing thickness,  $N_t$ , and FF progressively decreases in thickness due to the possibility of increased series resistance in thicker devices, leading to a reduction in FF. Furthermore, Fig. 5(d') shows that when the  $N_t$  was  $< 5 \times 10^{14} \text{ cm}^{-3}$  and the absorber thickness was  $\geq 2 \mu\text{m}$ , the corresponding highest PCE value of 30.10% is achieved. The PCE initially increases with thickness and reaches its maximum PCE at a thickness of 3  $\mu\text{m}$ . A linear relationship between the increase in thickness and the absorption of light leads to the generation of a greater number of electron–hole pairs. This increases the photocurrent and thus improves the efficiency of energy conversion. Consequently, the presence of excess PbI<sub>2</sub> on the perovskite layer leads to larger photovoltaic parameters. The optimizing perovskite layer thickness and defect density  $N_t$  results in the FF decrease from 71.60% to 26.20%, as shown in Fig. 5(c'). However, the FF presents a gradual decrease with increased 1.7  $\mu\text{m}$  to 3  $\mu\text{m}$  (in all this range of thickness with had found high performance of PSC) and  $N_t$  less than  $5 \times 10^{14} \text{ cm}^{-3}$ . The recombination directly affects the performances of the PSCs, and the recombination losses are due to defects in the materials.<sup>69</sup> Recombination losses limit the collection of the current and directly affect the current density and the voltage of the PSC.

**3.2.3 Impact of the radiative and auger recombination on photovoltaic performances.** The recombination directly affects the performances of the PSCs, and the recombination losses are certain due to defects in the materials.<sup>69</sup> Recombination losses limit the collection of the current and directly affect the current density and voltage of the PSC. To analyze the effect of the radiative and Auger recombination on the device performances, we varied the radiative recombination coefficient ( $B_{rad}$ ) from  $10^{-12}$  to  $10^{-7} \text{ cm}^3 \text{ s}^{-1}$ , and the Auger electron/hole recombination coefficient ( $B_{n/p}$ ), varied from  $10^{-28}$  to  $10^{-23} \text{ cm}^6 \text{ s}^{-1}$ , are represented as contour mapping, as shown in Fig. 6(a)–(d). The higher values of  $B_{rad}$  and  $B_{n/p}$  exhibit an adversative effect on the PV performances of the device. From Fig. 6(a)–(d), we observed a higher value of PCE (22.95%), FF (67.10%),  $V_{OC}$  (0.9765 V), and  $J_{SC}$  (35.05  $\text{mA cm}^{-2}$ ) at a lower value  $B_{rad}$  of  $10^{-12} \text{ cm}^3 \text{ s}^{-1}$ . The PCE of the decreased to 9.56% as  $B_{rad}$  increased to  $10^{-7} \text{ cm}^3 \text{ s}^{-1}$ . Otherwise, PSC exhibits higher performance at a high value of  $B_{n/p}$  Auger, where we observe that the effect of  $B_{n/p}$  Auger on the PSC performances is neglected compared to the effect of  $B_{rad}$ .<sup>66</sup> Consequently, the  $B_{rad}$  value in the range of  $10^{-12}$ – $10^{-10} \text{ cm}^3 \text{ s}^{-1}$  is suitable for higher PV performances, and the minimum performance occurs at a higher value of  $10^{-23} \text{ cm}^6 \text{ s}^{-1}$ . Compared with Auger recombination, radiative recombination is the dominant mechanism in perovskite solar cells due to their direct band gap large dielectric constant, which means that photon emission is very efficient *via* band-to-band transitions.<sup>70</sup> Owing to the passivation of perovskite by excess PbI<sub>2</sub>, we achieved high performance even in the presence of band-to-band recombination. Without passivation, the presence of band-to-band recombination results in lower performance.

**3.2.4 Impact of the interfacial defect density on the photovoltaic performances.** Interface defect density is a critical



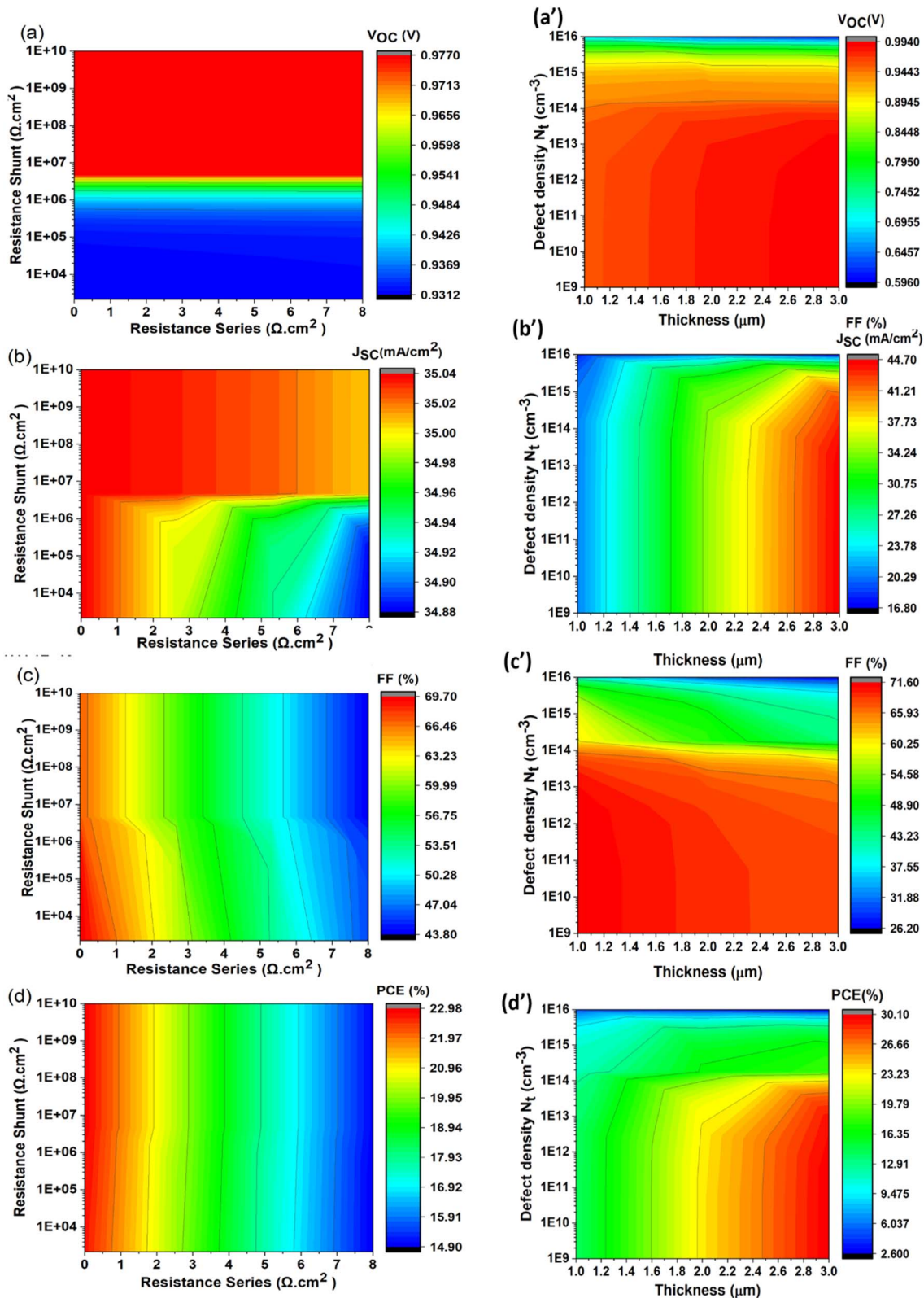


Fig. 5 Contour mapping of PSC performances illustrating the effect of the variation in series and shunt resistances on the performance of the PSC by  $V_{OC}$  (a),  $J_{SC}$  (b), FF (c), and PCE (d). Contour mapping of PSC performances by  $V_{OC}$  (a'),  $J_{SC}$  (b'), FF (c'), and PCE (d') with the variation in thickness and density defects  $N_t$  of the MAPbI<sub>3</sub> absorber layer.

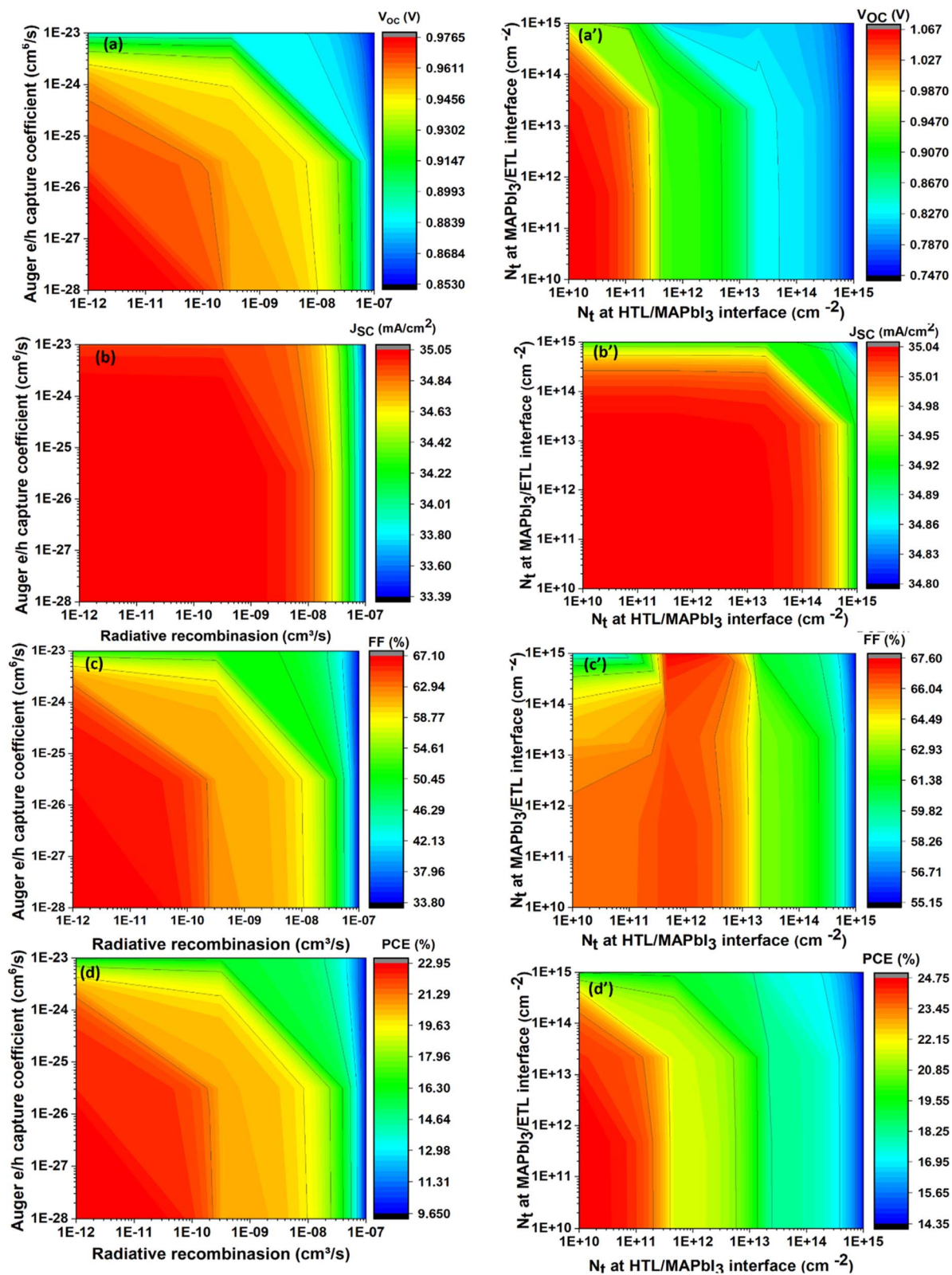


Fig. 6 Contour mapping representing the effect of the radiative recombination coefficient ( $cm^3 s^{-1}$ ) and Auger electron capture coefficient ( $cm^6 s^{-1}$ ) on the PSC performances: (a)  $V_{OC}$ , (b)  $J_{SC}$ , (c) FF and (d) PCE. The effect of interface defect density at the MAPbI<sub>3</sub>/SnO<sub>2</sub> interface and spiro-OMeTAD/MAPbI<sub>3</sub> interface is presented in (a')  $V_{OC}$ , (b')  $J_{SC}$ , (c') FF, and (d') PCE.



parameter influencing the performance of PSCs, as it directly affects interfacial recombination. Recombination occurring at the interfaces between the absorber and transport layers results in the formation of interface defect states. In our study, we systematically varied the interface defect density from  $10^{10}$   $\text{cm}^{-2}$  to  $10^{15}$   $\text{cm}^{-2}$  at the MAPbI<sub>3</sub>/SnO<sub>2</sub> and MAPbI<sub>3</sub>/spiro-OMeTAD interfaces to assess their impact on the photovoltaic performance of PSCs, as illustrated in Fig. 6(a')–(d'). These figures depict the contour mapping of defect density variations at the MAPbI<sub>3</sub>/SnO<sub>2</sub> and spiro-OMeTAD/MAPbI<sub>3</sub> interfaces, revealing that the highest PSC performances are achieved when the  $N_t$  ranges from  $10^{10}$  to  $10^{14}$   $\text{cm}^{-2}$ . Beyond this range ( $>10^{14}$   $\text{cm}^{-2}$ ), there is a slight decrease in PCE,  $J_{\text{SC}}$ , and  $V_{\text{OC}}$ , indicating suboptimal conditions. Specifically, the significant decrease in performance is attributed to higher recombination rates at the MAPbI<sub>3</sub>/spiro-OMeTAD interface. These findings underscore the critical importance of optimizing interface defect densities within the specified range to enhance the overall efficiency and stability of PSCs. Future research efforts should focus on further refining these interfaces to achieve even higher performance levels.<sup>71,72</sup>

**3.2.5 Impact of the work function of front and back contact on photovoltaic performances.** There are several studies in which the back metal work function (WF) has been varied to obtain better performance, but there are limited studies about the effect of WF on front contact. Herein, we reported the impact of WF on recent contacts (front and rear), such as aluminium-doped ZnO (AZO),<sup>73</sup> nanowire of silver with the introduction of gold and molybdenum oxides (AgNW–Au–MoO<sub>3</sub>)<sup>74</sup> and hydrogen-doped indium oxide deposited on ITO (IOH/ITO);<sup>75</sup> additionally, we reported the rear contacts, such as Au, nanowire of silver (NWs Ag), single-walled carbon nanotubes (SWCNTs),<sup>76,77</sup> and indium zinc oxide In<sub>2</sub>O<sub>3</sub>:Zn (IZO), the last one being recently used as a rear contact for semi-transparent solar cells.<sup>78,79</sup> The work functions of these

materials are extracted from the literature. Fig. 7 demonstrates that the WF of the back and front contacts varies from 4.3 eV to 5.4 eV and from 4.1 to 4.7 eV to illustrate the impact of the WF of both contacts on the performance of PSC. The PCE of our simulated solar cell with varying back and front contacts is shown in Fig. 7. The increasing work function of back contact increases the PSC performance, where the maximum PCE in its case is above 5.3 eV. This could be attributed to the MAPbI<sub>3</sub> work function (−5.46 eV), which saturates the efficiency, due to the alignment of the HTL work function and the valence band of the absorber layer. Using a high metal work function, the Fermi level energy decreases due to the band bending at the metal-semiconductor interface, making the contact more ohmic and the type of contact we attempt to achieve in PSC.<sup>80</sup> We assume that IZO could be used as a transparent back contact. Otherwise, in the front contact (see Fig. 7), the PCE decreases with the work function. This could be explained as follows: a front contact with a high work function leads to an increase in the interface recombination as an energy barrier prevents electron transfer into the front contact, and the occurrence of inverted band bending, which hinders charge transport and collection.<sup>81</sup> To aim to achieve optimal PSC performance, it is crucial to carefully choose a front contact with a work function slightly higher than the conduction band of absorber layer MAPbI<sub>3</sub> (~4.0 eV). In this case, the AZO is the best front contact for the PSC.

After using all the optimization values obtained previously, we hypothesize that the IZO and AZO with work functions of 5.3 eV and 4.19 eV, respectively, could be chosen as an effective alternative to replace the Au and ITO, respectively. An encouraging performance of PSC using these contacts is achieved by applying this structure AZO/SnO<sub>2</sub>/MAPbI<sub>3</sub> with excess PbI<sub>2</sub>/spiro-OMeTAD/IZO, giving  $V_{\text{OC}} = 1.08$  V,  $J_{\text{SC}} = 36.90$  mA  $\text{cm}^{-2}$ , FF = 65.16% and PCE = 26.03%. The introduction of IZO on PSC is reported for the first time by Wahl *et al.*,<sup>82</sup> where they demonstrated efficient inverted semi-transparent perovskite solar cells by implementing a sputtered IZO layer as TCO on organic electron transport layers without using a protective buffer layer with a PCE of around 13%. It could be improved with the introduction of a front metal contact with a low work function as demonstrated by our results.

Fig. 8 illustrates the photovoltaic performance of the MAPbI<sub>3</sub>-based perovskite solar cell, highlighting all key parameters. Our study demonstrates that incorporating a small excess of PbI<sub>2</sub> during the fabrication process leads to the formation of a passivation layer on the perovskite surface. This layer acts as a barrier, preventing ion migration, which is a common cause of performance degradation and instability in perovskite solar cells. The simulation results based on this simple synthesis method are promising, with an optimized device structure (AZO/SnO<sub>2</sub>/MAPbI<sub>3</sub> with excess PbI<sub>2</sub>/spiro-OMeTAD/IZO) achieving a PCE of 26%. Even prior to optimization, the initial device (ITO/SnO<sub>2</sub>/MAPbI<sub>3</sub>/spiro-OMeTAD/Au) shows a competitive PCE of 24%. These values are comparable to devices reported in the literature that use excess PbI<sub>2</sub> for passivation, yet our method simplifies the process and maintains high performance.

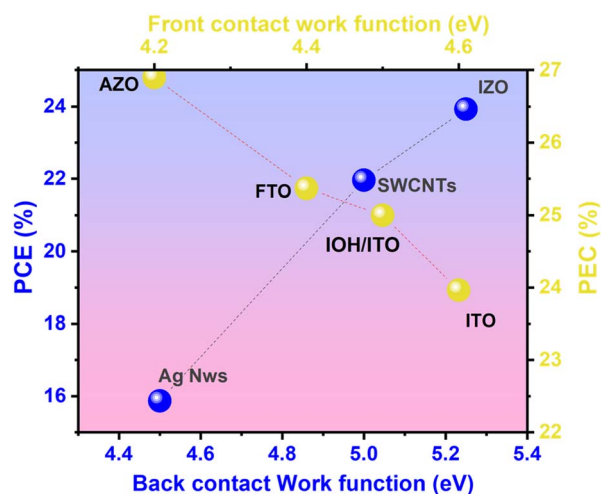


Fig. 7 Effect of the work function of different contacts (back and front contacts) on the power conversion efficiency of planar perovskite solar cells, MAPbI<sub>3</sub> as a perovskite absorber, SnO<sub>2</sub> as ETM and spiro-OMeTAD as HTL.



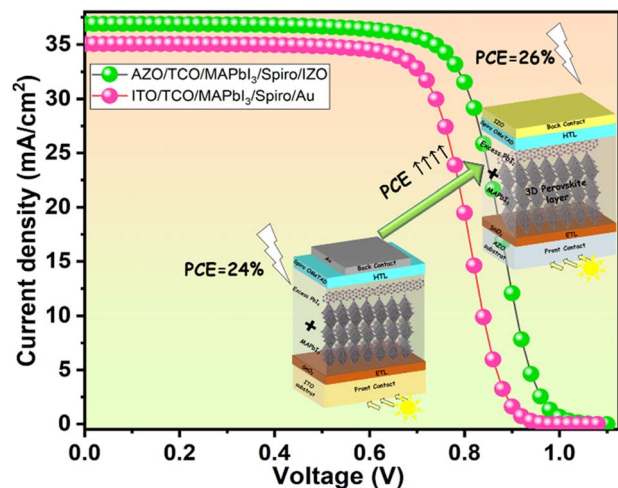


Fig. 8  $J$ - $V$  characteristics of the old and new architecture of the MAPbI<sub>3</sub>-based solar cell with the photovoltaic parameters, and the inset shows a schematic of design of the n-i-p structure for the PSC used in SCAPS simulation: AZO/SnO<sub>2</sub>/MAPbI<sub>3</sub> with excess PbI<sub>2</sub>/spiro-OMeTAD/IZO.

Table 2 summarizes the PV performance comparison of published experimental and theoretical works with the current work, explicitly using excess PbI<sub>2</sub> with AZO and IZO as front and rear contacts, respectively. The experimental and theoretical studies by Chen *et al.*<sup>48</sup> showed that PSCs with an *in situ* passivation using an excess PbI<sub>2</sub> device structure (ITO/SnO<sub>2</sub>/(FAPbI<sub>3</sub>)<sub>x-1</sub>(MAPbBr<sub>3</sub>)<sub>x</sub>/spiro-OMeTAD/Au) offer a PCE of ~19% even when they used perovskite material more stable than MAPbI<sub>3</sub>.

Similarly, Duan *et al.*<sup>59</sup> experimentally proved that the PSCs (ITO/SnO<sub>2</sub>/MAPbI<sub>3</sub>/spiro-OMeTAD/Ag) provide a good efficiency of 21.23%. The perovskite films were prepared by two-step

sequential deposition, excess PbI<sub>2</sub> was distributed on the surface of the perovskite film, and then a dual-functional surfactant (oleamide) was introduced to control the distribution of excess PbI<sub>2</sub> on the perovskite films. Even with the high PCE achieved by this device, the procedure of elaborating the MAPbI<sub>3</sub> is complex and expensive because of the chemical compounds used. Furthermore, Runnan Yu *et al.*<sup>13</sup> proved that the PbI<sub>2</sub> excess enhances the photovoltaic performance, achieving a PCE of 23.22% for (ITO/SnO<sub>2</sub>/FA<sub>0.92</sub>MA<sub>0.08</sub>PbI<sub>3</sub>/PEAI/HTL/MoO<sub>3</sub>/Ag) using a one-step process incorporated into PbI<sub>2</sub> an oxime acid-based material with multi-coordination sites and ethyl 2-(2-aminothiazole-4-yl)-2-hydroxyiminoacetate (EHA). Their results show that the choice of the one-step deposition process is effective and leads to good photovoltaic parameters. In a very recent development, Jiang *et al.*<sup>83</sup> employed IZO as a rear electrode and (2-(9H-carbazol-9-yl)ethyl) phosphonic acid (2PACz) to the passivation of the interface between the HTL and perovskite, which provided better stability with a higher PCE of 20.01%. Moreover, Wang *et al.*<sup>84</sup> proposed a method to improve the performance of PSCs by texturing the surface of the underlying AZO substrate, ultimately leading to a higher PCE of 17.6% for this textured device (AZO/SnO<sub>2</sub>/MAPbI<sub>3</sub>/spiro-OMeTAD/Ag). Without using any passivation of the perovskite/HTL interface. Dubey *et al.*<sup>73</sup> carried out experimental and simulation work of the PSC device (PET/AZO/ZnO-NRs/MASnI<sub>3</sub>:xLn<sup>3+</sup>/PTAA/Au), highlighting the promising potential of AZO as front contact and lanthanide ion doping in the absorbent layer as it has remarkably improved the photovoltaic performance of PSCs (25.85%).

The comparison of our results with the literature highlights the positive effect of an *in situ* passivating interface by an excess of PbI<sub>2</sub> using a one-step spin-coating method rather than depositing it as a separate thin layer beneath the perovskite or employing more complex deposition techniques, such as the

Table 2 Summary of the MAPbI<sub>3</sub>'s *in situ* passivation *via* spin-coating (one and two-step) reported in the literature

Device structure	Deposition method of the perovskite layer	V <sub>OC</sub> (V)	J <sub>SC</sub> (mA cm <sup>-2</sup> )	FF (%)	PCE (%)	Ref.
ITO/SnO <sub>2</sub> /perovskite/spiro-OMeTAD/Au	PbI <sub>2</sub> + organic salt	1.06	23.36	78.64	19.55	47
FTO/TiO <sub>2</sub> /MAPbI <sub>3</sub> /spiro-OMeTAD/Au	Spin-coated <i>via</i> a two-step process	1.08	23.30	65.50	16.5	51
	Excess PbI <sub>2</sub>					
ITO/SnO <sub>2</sub> /MAPbI <sub>3</sub> /spiro-OMeTAD/Ag	Spin-coated <i>via</i> a one-step process	1.17	24.39	81.00	23.12	55
	PbI <sub>2</sub> + oleamide					
ITO/SnO <sub>2</sub> /FA <sub>0.92</sub> MA <sub>0.08</sub> PbI <sub>3</sub> /PEAI/spiro-OMeTAD/MoO <sub>3</sub> /Ag	Spin-coated <i>via</i> a two-step process	1.16	25.41	78.77	23.22	13
	PbI <sub>2</sub> + EHA					
Glass/FTO/MeO-2PACz/CS <sub>0.05</sub> Rb <sub>0.05</sub>	Spin-coated <i>via</i> a one-step process	1.14	22.80	76.64	20.01	79
MA <sub>0.05</sub> FA <sub>0.85</sub> Pb(I <sub>0.95</sub> Br <sub>0.05</sub> ) <sub>3</sub> /LiF/C <sub>60</sub> /SnO <sub>2</sub> /IZO	Spin-coated <i>via</i> a two-step process	1.04	23.7	70	17.9	80
	No passivation					
AZO/SnO <sub>2</sub> /MAPbI <sub>3</sub> /spiro-OMeTAD/Ag	Spin-coated <i>via</i> a one-step process	1.04	23.7	70	17.9	80
	No passivation					
PET/AZO/ZnO-NRs/MASnI <sub>3</sub> :xLn <sup>3+</sup> /PTAA/Au	Spin-coated <i>via</i> a two-step process	1.34	22.08	86.83	25.84	69
	No passivation					
ITO/SnO <sub>2</sub> /MAPbI <sub>3</sub> /spiro-OMeTAD/Au	Spin-coated <i>via</i> a two-step process	1.00	35.04	68.01	23.93	This study
	PbI <sub>2</sub> excess					
AZO/SnO <sub>2</sub> /MAPbI <sub>3</sub> /spiro-OMeTAD/IZO	Spin-coated <i>via</i> a one-step process	1.08	36.90	65.16	26.03	This study
	PbI <sub>2</sub> excess					
	Spin-coated <i>via</i> a one-step process					



two-step spin-coating method. Furthermore, the choice of transparent electrodes and the good performance achieved opened the doors to semi-transparent perovskite solar cells (ST-PSCs), and its development faces several challenges.<sup>85</sup>

## 4. Conclusion

We correlated the experimental and theoretical investigations of the *in situ* passivation of the MAPbI<sub>3</sub> layer using a cost-effective one-step method of deposition by spin coating. The structural and optical characteristics are investigated. The tetragonal structure of the MAPbI<sub>3</sub> film is confirmed to be oriented along the (110) with an average size of ~179.8 nm. Moreover, the deposited MAPbI<sub>3</sub> presented a PbI<sub>2</sub> phase, which means there is a segregation of PbI<sub>2</sub> on the MAPbI<sub>3</sub> phase where it segregated at its GBs. However, the thickness of MAPbI<sub>3</sub> is above 2.02 μm. The band gap (1.53 eV) and the absorption coefficient ( $5 \times 10^3 \text{ cm}^{-1}$ ) of the MAPbI<sub>3</sub> absorber were extracted from the transmittance UV spectra, indicating a high absorption. Furthermore, the experiments are supported by theoretical calculations. The MAPbI<sub>3</sub>-based planar PSC (*i.e.*, ITO/SnO<sub>2</sub>/MAPbI<sub>3</sub> with excess PbI<sub>2</sub>/spiro-OMeTAD/Au) is conducted utilizing drift-diffusion SCAPS-1D simulations. The simulated PSC demonstrates a high efficiency of ~23.93%, surpassing other devices passivated using PbI<sub>2</sub> excess. The impact of  $R_s$  and  $R_{sh}$  on PSC performances is deeply investigated. Results show that  $R_s$  presents a negative impact on PSC performances while the  $R_{sh}$  reveals a positive impact. A study to find the optimum parameters of absorber thickness and defect density ( $N_c$ ), series and shunt resistances, radiative recombination coefficient, Auger hole/electron capture coefficient, and interfacial defect densities is carried out. In addition, the effects of changing the back and front contacts are investigated. The IZO and AZO are the most effective alternatives to replace the Au and ITO and give the highest performance. Even with the most unstable lead-halide perovskite (MAPbI<sub>3</sub>), the final PCE is optimized to be 26.03%, which is an encouraging result and turns attention to the ST-PSCs. We believe that our work could provide an alternative way to enhance experimentally the efficiency of lead-halide perovskites-based solar cells using a simple method of depositing and passivating the interface between MAPbI<sub>3</sub> and HTL, which is the main cause of decreasing the PCE of PSCs. As well, our results could help integrate perovskites on III–V class substrates such as GaAs, GaN and their derivative compounds.

## Data availability

The data that support the findings of this study are available in the ESI† of this article.

## Conflicts of interest

There are no conflicts to declare.

## Acknowledgements

This project has received funding from the European Union's Horizon 2020 Research and Innovation Program under the Marie Skłodowska-Curie Project OPTOHYB with grant agreement no. 1010233335 (recipient: Tarak Hidouri). The authors would like to thank Marc Burgelman, University of Gent, Belgium, for providing free access to drift-diffusion SCAPS-1D simulation software.

## References

- 1 J. Yuan, A. Hazarika, Q. Zhao, X. Ling, T. Moot, W. Ma and J. M. Luther, Metal Halide Perovskites in Quantum Dot Solar Cells: Progress and Prospects, *Joule*, 2020, 4(6), 1160–1185, DOI: [10.1016/j.joule.2020.04.006](https://doi.org/10.1016/j.joule.2020.04.006).
- 2 F. H. Isikgor, S. Zhumagali, L. V. Luis, M. De Bastiani, I. McCulloch and S. De Wolf, Molecular Engineering of Contact Interfaces for High-Performance Perovskite Solar Cells, *Nat. Rev. Mater.*, 2023, 8, 89–108, DOI: [10.1038/s41578-022-00503-3](https://doi.org/10.1038/s41578-022-00503-3).
- 3 H. Chen, A. Maxwell, C. Li, S. Teale, B. Chen, T. Zhu, E. Ugur, G. Harrison, L. Grater, J. Wang, Z. Wang, L. Zeng, S. M. Park, L. Chen, P. Serles, R. A. Awni, B. Subedi, X. Zheng, C. Xiao, N. J. Podraza, T. Filleter, C. Liu, Y. Yang, J. M. Luther, S. De Wolf, M. G. Kanatzidis, Y. Yan and E. H. Sargent, Regulating Surface Potential Maximizes Voltage in All-Perovskite Tandems, *Nature*, 2023, 613(7945), 676–681, DOI: [10.1038/s41586-022-05541-z](https://doi.org/10.1038/s41586-022-05541-z).
- 4 J. Park, J. Kim, H. S. Yun, M. J. Paik, E. Noh, H. J. Mun, M. G. Kim, T. J. Shin and S. Il Seok, Supplimentary Information: Controlled Growth of Perovskite Layers with Volatile Alkylammonium Chlorides, *Nature*, 2023, 616(7958), 724–730, DOI: [10.1038/s41586-023-05825-y](https://doi.org/10.1038/s41586-023-05825-y).
- 5 M. C. Brennan, A. Forde, M. Zhukovskyi, A. J. Baublis, Y. V. Morozov, S. Zhang, Z. Zhang, D. S. Kilin and M. Kuno, Universal Size-Dependent Stokes Shifts in Lead Halide Perovskite Nanocrystals, *J. Phys. Chem. Lett.*, 2020, 11(13), 4937–4944, DOI: [10.1021/acs.jpclett.0c01407](https://doi.org/10.1021/acs.jpclett.0c01407).
- 6 B. Xia, M. Tu, B. Pradhan, F. Ceyssens, M. L. Tietze, V. Rubio-Giménez, N. Wauteraerts, Y. Gao, M. Kraft, J. A. Steele, E. Debroye, J. Hofkens and R. Ameloot, Flexible Metal Halide Perovskite Photodetector Arrays via Photolithography and Dry Lift-Off Patterning, *Adv. Eng. Mater.*, 2022, 24(1), 2100930, DOI: [10.1002/adem.202100930](https://doi.org/10.1002/adem.202100930).
- 7 G. S. Kumar, P. K. Sarkar, B. Pradhan, M. Hossain, K. D. M. Rao and S. Acharya, Large-Area Transparent Flexible Guanidinium Incorporated MAPbI<sub>3</sub> Microstructures for High-Performance Photodetectors with Enhanced Stability, *Nanoscale Horiz.*, 2020, 5(4), 696–704, DOI: [10.1039/c9nh00774a](https://doi.org/10.1039/c9nh00774a).
- 8 H. Shahivandi, M. Vaezzadeh and M. Saeidi, Solar Energy Materials and Solar Cells Study of the Effect of Temperature on Light-Induced Degradation in Methylammonium Lead Iodine Perovskite Solar Cells, *Sol. Energy Mater. Sol. Cells*, 2020, 218(September), 110770, DOI: [10.1016/j.solmat.2020.110770](https://doi.org/10.1016/j.solmat.2020.110770).



- 9 M. B. Islam, M. Yanagida, Y. Shirai, Y. Nabetani and K. Miyano, Highly Stable Semi-Transparent MAPbI<sub>3</sub> Perovskite Solar Cells with Operational Output for 4000 h, *Sol. Energy Mater. Sol. Cells*, 2019, **195**(March), 323–329, DOI: [10.1016/j.solmat.2019.03.004](https://doi.org/10.1016/j.solmat.2019.03.004).
- 10 Z. Dai, M. C. Doyle, X. Liu, M. Hu, Q. Wang, C. E. Athanasiou, Y. Liu, B. W. Sheldon, H. Gao, S. Liu and N. P. Padture, The Mechanical Behavior of Metal-Halide Perovskites: Elasticity, Plasticity, Fracture, and Creep, *Scr. Mater.*, 2023, **223**(August 2022), 115064, DOI: [10.1016/j.scriptamat.2022.115064](https://doi.org/10.1016/j.scriptamat.2022.115064).
- 11 Z. Dai, S. K. Yadavalli, M. Hu, M. Chen, Y. Zhou and N. P. Padture, Effect of Grain Size on the Fracture Behavior of Organic-Inorganic Halide Perovskite Thin Films for Solar Cells, *Scripta Mater.*, 2020, **185**, 47–50, DOI: [10.1016/j.scriptamat.2020.03.044](https://doi.org/10.1016/j.scriptamat.2020.03.044).
- 12 D. H. Kang, C. Ma and N. G. Park, Antiseptic Povidone-Iodine Heals the Grain Boundary of Perovskite Solar Cells, *ACS Appl. Mater. Interfaces*, 2022, **14**(7), 8984–8991, DOI: [10.1021/acsmi.1c21479](https://doi.org/10.1021/acsmi.1c21479).
- 13 R. Yu, G. Wu, R. Shi, Z. Ma, Q. Dang, Y. Qing, C. Zhang, K. Xu and Z. Tan, Multidentate Coordination Induced Crystal Growth Regulation and Trap Passivation Enables over 24% Efficiency in Perovskite Solar Cells, *Adv. Energy Mater.*, 2023, **13**(1), 1–10, DOI: [10.1002/aenm.202203127](https://doi.org/10.1002/aenm.202203127).
- 14 Z. Jiang, D. Wang, J. Sun, B. Hu, L. Zhang, X. Zhou, J. Wu, H. Hu, J. Zhang, W. C. H. Choy and B. Xu, Quenching Detrimental Reactions and Boosting Hole Extraction via Multifunctional NiOx/Perovskite Interface Passivation for Efficient and Stable Inverted Solar Cells, *Small Methods*, 2023, **2300241**, 1–9, DOI: [10.1002/smt.202300241](https://doi.org/10.1002/smt.202300241).
- 15 P. Zhao, B. J. Kim and H. S. Jung, Passivation in Perovskite Solar Cells: A Review, *Mater. Today Energy*, 2018, **7**, 267–286, DOI: [10.1016/j.mtener.2018.01.004](https://doi.org/10.1016/j.mtener.2018.01.004).
- 16 Z. Gozukara Karabag, A. Karabag, U. Gunes, X. X. Gao, O. A. Syzgenteva, M. A. Syzgenteva, F. Varlioglu Yaylali, N. Shibayama, H. Kanda, A. I. Rafieh, R. C. Turnell-Ritson, P. J. Dyson, S. Yerci, M. K. Nazeeruddin and G. Gunbas, Tuning 2D Perovskite Passivation: Impact of Electronic and Steric Effects on the Performance of 3D/2D Perovskite Solar Cells, *Adv. Energy Mater.*, 2023, 1–10, DOI: [10.1002/aenm.202302038](https://doi.org/10.1002/aenm.202302038).
- 17 E. Shirzadi, F. Ansari, H. Jinno, S. Tian, O. Ouellette, F. T. Eickemeyer, B. Carlsen, A. Van Muyden, H. Kanda, N. Shibayama, F. F. Tirani, M. Grätzel, A. Hagfeldt, M. K. Nazeeruddin and P. J. Dyson, High-Work-Function 2D Perovskites as Passivation Agents in Perovskite Solar Cells, *ACS Energy Lett.*, 2023, **8**(9), 3955–3961, DOI: [10.1021/acsenenergylett.3c01326](https://doi.org/10.1021/acsenenergylett.3c01326).
- 18 S. Sajid, S. Alzahmi, N. Tabet, Y. Haik and I. M. Obaidat, Fabricating Planar Perovskite Solar Cells through a Greener Approach, *Nanomaterials*, 2024, **14**(7), 594, DOI: [10.3390/nano14070594](https://doi.org/10.3390/nano14070594).
- 19 S. Rabhi, T. A. Hameed, S. Mayarambakam, M. K. Hossain and K. Sekar, The Impact of CBz-PAI Interlayer in Various HTL-Based Flexible Perovskite Solar Cells: A Drift-Diffusion Numerical Study, *Heliyon*, 2024, **10**, 1–12, DOI: [10.1016/j.heliyon.2024.e31138](https://doi.org/10.1016/j.heliyon.2024.e31138).
- 20 G. F. I. Toki, M. K. Hossain, M. Shihab Uddin, A. M. Tawfeek, S. Rabhi, M. A. Darwish, R. Haldhar, D. K. Dwivedi, J. Madan and R. Pandey, Unveiling the Potential of Lead-Free Cs<sub>2</sub>AgBi<sub>0.75</sub>Sb<sub>0.25</sub>Br<sub>6</sub> Double Perovskite Solar Cells with Multilayer Charge Transport for 30% Efficiency, *Inorg. Chem. Commun.*, 2024, **165**(November 2023), 112439, DOI: [10.1016/j.inoche.2024.112439](https://doi.org/10.1016/j.inoche.2024.112439).
- 21 V. Biju, L. Chouhan, S. Ito, E. M. Thomas, Y. Takano, S. Ghimire and H. Miyasaka, Real-Time Blinking Suppression of Perovskite Quantum Dots by Halide Vacancy Filling, *ACS Nano*, 2021, **15**(2), 2831–2838, DOI: [10.1021/acsnano.0c08802](https://doi.org/10.1021/acsnano.0c08802).
- 22 Y. Wang, D. F. Ruiz Diaz, K. S. Chen, Z. Wang and X. C. Adroher, Materials, Technological Status, and Fundamentals of PEM Fuel Cells – A Review, *Mater. Today*, 2020, **32**(February), 178–203, DOI: [10.1016/j.mattod.2019.06.005](https://doi.org/10.1016/j.mattod.2019.06.005).
- 23 S. M. Majeed, M. K. A. Mohammed and D. S. Ahmed, Efficient and Stable Hole-Transporting-Layer-Free Perovskite Solar Cells by Introducing Propionyl Chloride Passivator, *Appl. Phys. A: Mater. Sci. Process.*, 2023, **129**(7), 1–9, DOI: [10.1007/s00339-023-06749-0](https://doi.org/10.1007/s00339-023-06749-0).
- 24 S. Rabhi, H. Benzouid, A. Slami and K. Dadda, Modeling and Numerical Simulation of a CH<sub>3</sub>NH<sub>3</sub>SnI<sub>3</sub> Perovskite Solar Cell Using the SCAPS1-D Simulator, *Eng. Proc.*, 2023, **56**(97), 1–7, DOI: [10.3390/ASEC2023-15300](https://doi.org/10.3390/ASEC2023-15300).
- 25 Y. Tidhar, E. Edri, H. Weissman, D. Zohar, G. Hodes, D. Cahen, B. Rybtchinski and S. Kirmayer, Crystallization of Methyl Ammonium Lead Halide Perovskites: Implications for Photovoltaic Applications, *J. Am. Chem. Soc.*, 2014, **136**, 13249–13256, DOI: [10.1021/ja505556s](https://doi.org/10.1021/ja505556s).
- 26 J. H. Heo, S. H. Im, J. H. Noh, T. N. Mandal, C. Lim, J. A. Chang, Y. H. Lee, H. Kim, A. Sarkar, K. Nazeeruddin and M. Gra, Efficient Inorganic–Organic Hybrid Heterojunction Solar Cells Containing Perovskite Compound and Polymeric Hole Conductors, *Nat. Photonics*, 2013, (May), 1–6, DOI: [10.1038/NPHOTON.2013.80](https://doi.org/10.1038/NPHOTON.2013.80).
- 27 S. Liu, V. P. Biju, Y. Qi, W. Chen and Z. Liu, Recent Progress in the Development of High-Efficiency Inverted Perovskite Solar Cells, *NPG Asia Mater.*, 2023, **15**(1), 27, DOI: [10.1038/s41427-023-00474-z](https://doi.org/10.1038/s41427-023-00474-z).
- 28 A. A. B. Baloch, M. I. Hossain, N. Tabet and F. H. Alharbi, Practical Efficiency Limit of Methylammonium Lead Iodide Perovskite (CH<sub>3</sub>NH<sub>3</sub>PbI<sub>3</sub>) Solar Cells, *J. Phys. Chem. Lett.*, 2018, **9**(2), 426–434, DOI: [10.1021/acs.jpcclett.7b03343](https://doi.org/10.1021/acs.jpcclett.7b03343).
- 29 E. Karimi and S. M. B. Ghorashi, Simulation of Perovskite Solar Cell with P<sub>3</sub>HT Hole-Transporting Materials, *J. Nanophotonics*, 2017, **11**, 1–15, DOI: [10.1117/1.jnp.11.032510](https://doi.org/10.1117/1.jnp.11.032510).
- 30 M. S. Rahman, S. Miah, M. S. W. Marma and T. Sabrina, Simulation Based Investigation of Inverted Planar Perovskite Solar Cell with All Metal Oxide Inorganic Transport Layers, in *2nd International Conference on Electrical, Computer and Communication Engineering, ECCE 2019*, 2019, pp. 1–7, DOI: [10.1109/ECACE.2019.8679283](https://doi.org/10.1109/ECACE.2019.8679283).



- 31 S. M. Hasnain, Examining the Advances, Obstacles, and Achievements of Tin-Based Perovskite Solar Cells: A Review, *Sol. Energy*, 2023, **262**(May), 111825, DOI: [10.1016/j.solener.2023.111825](https://doi.org/10.1016/j.solener.2023.111825).
- 32 S. Karthick, S. Velumani and J. Bouclé, Experimental and SCAPS Simulated Formamidinium Perovskite Solar Cells: A Comparison of Device Performance, *Sol. Energy*, 2020, **205**(March), 349–357, DOI: [10.1016/j.solener.2020.05.041](https://doi.org/10.1016/j.solener.2020.05.041).
- 33 P. Schulz, D. Cahen and A. Kahn, Halide Perovskites: Is It All about the Interfaces?, *Chem. Rev.*, 2019, **119**(5), 3349–3417, DOI: [10.1021/acs.chemrev.8b00558](https://doi.org/10.1021/acs.chemrev.8b00558).
- 34 P. Tiwari, M. F. Alotaibi, Y. Al-Hadeethi, V. Srivastava, B. Arkook, P. Sadanand, P. Lohia, D. K. Dwivedi, A. Umar, H. Algadi and S. Baskoutas, Design and Simulation of Efficient SnS-Based Solar Cell Using Spiro-OMeTAD as Hole Transport Layer, *Nanomaterials*, 2022, **12**(14), 1–9, DOI: [10.3390/nano12142506](https://doi.org/10.3390/nano12142506).
- 35 M. D. Shahjahan, T. Okamoto, L. Chouhan, B. M. Sachith, N. Pradhan, H. Misawa and V. Biju, Halide Perovskite Single Crystals and Nanocrystal Films as Electron Supplementary Information for Halide Perovskite Single Crystals and Nanocrystal Films As, *Angew. Chem., Int. Ed.*, 2023, **64**(4), e202215947, DOI: [10.1002/anie.202215947](https://doi.org/10.1002/anie.202215947).
- 36 T. Minemoto and M. Murata, Theoretical Analysis on Effect of Band Offsets in Perovskite Solar Cells, *Sol. Energy Mater. Sol. Cells*, 2015, **133**, 8–14, DOI: [10.1016/j.solmat.2014.10.036](https://doi.org/10.1016/j.solmat.2014.10.036).
- 37 M. Serhan, M. Sprowls, D. Jackemeyer, M. Long, I. D. Perez, W. Maret, N. Tao and E. Forzani, Interface Engineering for High-Performance Perovskite Hybrid Solar Cells, *J. Mater. Chem. A*, 2015, **3**, 19205–19217, DOI: [10.1039/x0xx00000x](https://doi.org/10.1039/x0xx00000x).
- 38 S. Y. Bang, Y. H. Suh, X. B. Fan, D. W. Shin, S. Lee, H. W. Choi, T. H. Lee, J. Yang, S. Zhan, W. Harden-Chaters, C. Samarakoon, L. G. Occhipinti, S. D. Han, S. M. Jung and J. M. Kim, Technology Progress on Quantum Dot Light-Emitting Diodes for next-Generation Displays, *Nanoscale Horiz.*, 2021, **6**(2), 68–77, DOI: [10.1039/d0nh00556h](https://doi.org/10.1039/d0nh00556h).
- 39 L. Calió, S. Kazim, M. Grätzel and S. Ahmad, Hole-Transport Materials for Perovskite Solar Cells, *Angew. Chem., Int. Ed.*, 2016, **55**(47), 14522–14545, DOI: [10.1002/anie.201601757](https://doi.org/10.1002/anie.201601757).
- 40 I. Belaidi, F. Khelfaoui, N. Attaf, A. Azzizi and M. S. Aida, Solvent and Spinning Speed Effects on CH<sub>3</sub>NH<sub>3</sub>PbI<sub>3</sub> Films Deposited by Spin Coating, *Phys. Status Solidi A*, 2019, 1–9, DOI: [10.1002/pssa.201900340](https://doi.org/10.1002/pssa.201900340).
- 41 M. K. Hossain, M. H. K. Rubel, G. F. I. Toki, I. Alam, M. F. Rahman and H. Bencherif, Effect of Various Electron and Hole Transport Layers on the Performance of CsPbI<sub>3</sub>-Based Perovskite Solar Cells: A Numerical Investigation in DFT, SCAPS-1D, and WxAMPS Frameworks, *ACS Omega*, 2022, **7**(47), 43210–43230, DOI: [10.1021/acsomega.2c05912](https://doi.org/10.1021/acsomega.2c05912).
- 42 Y. Raoui, H. Ez-Zahraoui, N. Tahiri, O. El Bounagui, S. Ahmad and S. Kazim, Performance Analysis of MAPbI<sub>3</sub> Based Perovskite Solar Cells Employing Diverse Charge Selective Contacts: Simulation Study, *Sol. Energy*, 2019, **193**(October), 948–955, DOI: [10.1016/j.solener.2019.10.009](https://doi.org/10.1016/j.solener.2019.10.009).
- 43 N. R. Pochont and Y. R. Sekhar, Numerical Simulation of Nitrogen-Doped Titanium Dioxide as an Inorganic Hole Transport Layer in Mixed Halide Perovskite Structures Using SCAPS 1-D, *Inorganics*, 2023, **11**(1), 1–17, DOI: [10.3390/inorganics11010003](https://doi.org/10.3390/inorganics11010003).
- 44 N. Taylor, E. Dunlop, F. Fabero, G. Friesen, W. Herrmann and J. Hohl-Ebinger, *Guidelines for PV Power Measurement in Industry*, Ispra, 2010, DOI: [10.2788/90247](https://doi.org/10.2788/90247).
- 45 E. N. Vincent Mercy, D. Srinivasan and L. Marasamy, Emerging BaZrS<sub>3</sub> and Ba(Zr,Ti)S<sub>3</sub> Chalcogenide Perovskite Solar Cells: A Numerical Approach Toward Device Engineering and Unlocking Efficiency, *ACS Omega*, 2024, **4**, 4359–4376, DOI: [10.1021/acsomega.3c06627](https://doi.org/10.1021/acsomega.3c06627).
- 46 S. Rabhi, K. Sekar, K. Kalna, Y. I. Bouderbala, N. Bouri, N. Oueldna, N. Belbachir, K. Dadda, M. S. Aida and N. Attaf, Experimental Findings and SCAPS-1D Simulations for High-Efficiency MAPbI<sub>3</sub> Perovskite Solar Cells beyond 31%, *Opt. Quantum Electron.*, 2024, **56**(1372), 2–23, DOI: [10.1007/s11082-024-07282-x](https://doi.org/10.1007/s11082-024-07282-x).
- 47 L. A. Muscarella, E. M. Hutter, S. Sanchez, C. D. Dieleman, T. J. Savenije, A. Hagfeldt, M. Saliba and B. Ehrler, Crystal Orientation and Grain Size: Do They Determine Optoelectronic Properties of MAPbI<sub>3</sub> Perovskite?, *J. Phys. Chem. Lett.*, 2019, **10**(20), 6010–6018, DOI: [10.1021/acs.jpclett.9b02757](https://doi.org/10.1021/acs.jpclett.9b02757).
- 48 Y. Chen, Q. Meng, Y. Xiao, X. Zhang, J. Sun, C. B. Han, H. Gao, Y. Zhang, Y. Lu and H. Yan, Mechanism of PbI<sub>2</sub> in Situ Passivated Perovskite Films for Enhancing the Performance of Perovskite Solar Cells, *ACS Appl. Mater. Interfaces*, 2019, **11**(47), 44101–44108, DOI: [10.1021/acsmi.9b13648](https://doi.org/10.1021/acsmi.9b13648).
- 49 P. Terpstra and H. G. K. Westenbrink, On the Crystal-Structure of Lead-Iodide, *Proc. Koninklijke Nederl. Akademie Wetenschappen*, 1926, **29**, 431–442.
- 50 N. N. Udalova, A. S. Tutantsev, S. A. Fateev, E. A. Zharenova, N. A. Belich, E. M. Nemygina, A. V. Ryabova, E. A. Goodilin and A. B. Tarasov, Crystallization Features of MAPbI<sub>3</sub> Hybrid Perovskite during the Reaction of PbI<sub>2</sub> with Reactive Polyiodide Melts, *Russ. J. Inorg. Chem.*, 2021, **66**(2), 153–162, DOI: [10.1134/S0036023621020200](https://doi.org/10.1134/S0036023621020200).
- 51 T. M. Brenner, Y. Rakita, Y. Orr, E. Klein, I. Feldman, M. Elbaum, D. Cahen and G. Hodes, Conversion of Single Crystalline PbI<sub>2</sub> to CH<sub>3</sub>NH<sub>3</sub>PbI<sub>3</sub>: Structural Relations and Transformation Dynamics, *Chem. Mater.*, 2016, **28**(18), 6501–6510, DOI: [10.1021/acs.chemmater.6b01747](https://doi.org/10.1021/acs.chemmater.6b01747).
- 52 A. Kojima, K. Teshima, Y. Shirai and T. Miyasaka, Organometal Halide Perovskites as Visible-Light Sensitizers for Photovoltaic Cells, *J. Am. Chem. Soc.*, 2009, **131**(17), 6050–6051, DOI: [10.1021/ja809598r](https://doi.org/10.1021/ja809598r).
- 53 G. H. Jaffari, M. Gul, A. M. Iqbal, W. Ali, W. Mahmood and A. Ali, Effect of Temperature on Structural Phase Transition and Photoluminescence in Organic-Inorganic Hybrid CH<sub>3</sub>NH<sub>3</sub>PbI<sub>3</sub>-XCl<sub>x</sub> Perovskite, *Opt. Mater.*, 2023, **142**(June), 114004, DOI: [10.1016/j.optmat.2023.114004](https://doi.org/10.1016/j.optmat.2023.114004).
- 54 Q. Chen, H. Zhou, T. B. Song, S. Luo, Z. Hong, H. S. Duan, L. Dou, Y. Liu and Y. Yang, Controllable Self-Induced Passivation of Hybrid Lead Iodide Perovskites toward High



- Performance Solar Cells, *Nano Lett.*, 2014, **14**(7), 4158–4163, DOI: [10.1021/nl501838y](https://doi.org/10.1021/nl501838y).
- 55 J. Zhang, X. Li, L. Wang, J. Yu, S. Wageh and A. A. Al-Ghamdi, Enhanced Performance of CH<sub>3</sub>NH<sub>3</sub>PbI<sub>3</sub> Perovskite Solar Cells by Excess Halide Modification, *Appl. Surf. Sci.*, 2021, **564**(June), 150464, DOI: [10.1016/j.apsusc.2021.150464](https://doi.org/10.1016/j.apsusc.2021.150464).
- 56 Q. Sun, X. Gong, H. Li, S. Liu, X. Zhao, Y. Shen and M. Wang, Direct Formation of I<sup>3-</sup> Ions in Organic Cation Solution for Efficient Perovskite Solar Cells, *Sol. Energy Mater. Sol. Cells*, 2018, **185**(April), 111–116, DOI: [10.1016/j.solmat.2018.05.017](https://doi.org/10.1016/j.solmat.2018.05.017).
- 57 R. Xu, F. Pan, J. Chen, J. Li, Y. Yang, Y. Sun, X. Zhu, P. Li, X. Cao, J. Xi, J. Xu, F. Yuan, J. Dai, C. Zuo, L. Ding, H. Dong, A. K. Y. Jen and Z. Wu, Optimizing the Buried Interface in Flexible Perovskite Solar Cells to Achieve Over 24% Efficiency and Long-Term Stability, *Adv. Mater.*, 2023, **2308039**, 1–12, DOI: [10.1002/adma.202308039](https://doi.org/10.1002/adma.202308039).
- 58 Z. Li, M. Yang, J. S. Park, S. H. Wei, J. J. Berry and K. Zhu, Stabilizing Perovskite Structures by Tuning Tolerance Factor: Formation of Formamidinium and Cesium Lead Iodide Solid-State Alloys, *Chem. Mater.*, 2016, **28**(1), 284–292, DOI: [10.1021/acs.chemmater.5b04107](https://doi.org/10.1021/acs.chemmater.5b04107).
- 59 G. Duan, W. Zhang, Y. Huang, W. Yu, X. Zhou, F. Wen, Y. Shang, Q. Chen, L. Yu, X. Hu, Y. Zhang, R. S. Bobba, S. Mabrouk, S. Yang, F. Liu and Q. Qiao, Regulate Excess PbI<sub>2</sub> Distribution on Perovskite Film via Amphiphilic Surfactant for Efficient and Stable Device, *Electrochim. Acta*, 2023, **462**(June), 142738, DOI: [10.1016/j.electacta.2023.142738](https://doi.org/10.1016/j.electacta.2023.142738).
- 60 P. Makuła, M. Pacia and W. Macyk, How To Correctly Determine the Band Gap Energy of Modified Semiconductor Photocatalysts Based on UV-Vis Spectra, *J. Phys. Chem. Lett.*, 2018, **9**(23), 6814–6817, DOI: [10.1021/acs.jpcclett.8b02892](https://doi.org/10.1021/acs.jpcclett.8b02892).
- 61 H. Sohrabpoor, M. Elyasi, M. Aldosari and N. E. Gorji, Modeling the PbI<sub>2</sub> Formation in Perovskite Solar Cells Using XRD/XPS Patterns, *Superlattices Microstruct.*, 2016, **97**, 556–561, DOI: [10.1016/j.spmi.2016.07.026](https://doi.org/10.1016/j.spmi.2016.07.026).
- 62 Y. Chen, Q. Meng, Y. Xiao, X. Zhang, J. Sun, C. B. Han, H. Gao, Y. Zhang, Y. Lu and H. Yan, Supporting Information: Mechanism of PbI<sub>2</sub> in Situ Passivated Perovskite Films for Enhancing the Performance of Perovskite Solar Cells, *ACS Appl. Mater. Interfaces*, 2019, **11**(47), 44101–44108, DOI: [10.1021/acsami.9b13648](https://doi.org/10.1021/acsami.9b13648).
- 63 Y. Huang, G. Yu, D. Khan, S. Wang, Y. Sui, X. Yang, Y. Zhuang, J. Tang, H. Gao, M. Xin, A. Aierken and Z. Tang, A Functional Biological Molecule Restores the PbI<sub>2</sub> Residue-Induced Defects in Two-Step Fabricated Perovskites, *Molecules*, 2023, **28**(7120), 1–11.
- 64 M. Abderrezek, *Modélisation Des Cellules Solaires Tandem à Couches Minces et à Haut Rendement*, UNIVERSITE SETIF-1, 2015.
- 65 A. K. Al-Mousoi, M. K. A. Mohammed, R. Pandey, J. Madan, D. Dastan, G. Ravi, P. Sakthivel and G. Anandha babu, Simulation and Analysis of Lead-Free Perovskite Solar Cells Incorporating Cerium Oxide as Electron Transporting Layer, *RSC Adv.*, 2022, **12**(50), 32365–32373, DOI: [10.1039/d2ra05957f](https://doi.org/10.1039/d2ra05957f).
- 66 S. R. Hosseini, M. Bahramgour, P. Yardani Sefidi, A. Tabatabaei Mashayekh, A. Moradi, N. Delibas, M. G. Hosseini and A. Niaei, Investigating the Effect of Non-Ideal Conditions on the Performance of a Planar CH<sub>3</sub>NH<sub>3</sub>PbI<sub>3</sub>-Based Perovskite Solar Cell through SCAPS-1D Simulation, *Heliyon*, 2022, **8**(11), 1–8, DOI: [10.1016/j.heliyon.2022.e11471](https://doi.org/10.1016/j.heliyon.2022.e11471).
- 67 Z. Omarova, D. Yerezhap, A. Aldiyarov and N. Tokmoldin, In Silico Investigation of the Impact of Hole-Transport Layers on the Performance of CH<sub>3</sub>NH<sub>3</sub>SnI<sub>3</sub> Perovskite Photovoltaic Cells, *Crystals*, 2022, **12**(5), 699, DOI: [10.3390/cryst12050699](https://doi.org/10.3390/cryst12050699).
- 68 M. Daboczi, I. Hamilton, S. Xu, J. Luke, S. Limbu, J. Lee, M. A. McLachlan, K. Lee, J. R. Durrant, I. D. Baikié and J. S. Kim, Origin of Open-Circuit Voltage Losses in Perovskite Solar Cells Investigated by Surface Photovoltage Measurement, *ACS Appl. Mater. Interfaces*, 2019, **11**(50), 46808–46817, DOI: [10.1021/acsami.9b16394](https://doi.org/10.1021/acsami.9b16394).
- 69 Y. Yalcinkaya, P. N. Rohrbeck, E. R. Schütz, A. Fakharuddin, L. Schmidt-Mende and S. A. L. Weber, Nanoscale Surface Photovoltage Spectroscopy, *Adv. Opt. Mater.*, 2023, **2301318**, 1–12, DOI: [10.1002/adom.202301318](https://doi.org/10.1002/adom.202301318).
- 70 A. Hajjiah, COMSOL Simulation of Non-Radiative Recombination Heat and Joule Heat in CZTSSe Thin Film Solar Cells, *Micro Nanostruct.*, 2022, **168**(March), 207313, DOI: [10.1016/j.micrna.2022.207313](https://doi.org/10.1016/j.micrna.2022.207313).
- 71 J. Zhuang, P. Mao, Y. Luan, N. Chen, X. Cao, G. Niu, F. Jia, F. Wang, S. Cao and J. Wang, Rubidium Fluoride Modified SnO<sub>2</sub> for Planar N-i-p Perovskite Solar Cells, *Adv. Funct. Mater.*, 2021, **31**(17), 1–8, DOI: [10.1002/adfm.202010385](https://doi.org/10.1002/adfm.202010385).
- 72 A. S. Chouhan, N. P. Jasti and S. Avasthi, Effect of Interface Defect Density on Performance of Perovskite Solar Cell: Correlation of Simulation and Experiment, *Mater. Lett.*, 2018, **221**, 150–153, DOI: [10.1016/j.matlet.2018.03.095](https://doi.org/10.1016/j.matlet.2018.03.095).
- 73 C. Dubey, D. K. Jarwal, H. Kumar, Y. Kumar, K. Mummaneni and G. Rawat, Development of Highly Efficient ZnO Nanorod-Based Nontoxic Perovskite Solar Cell Using AZO Buffer Layer and Lanthanide Doping, *IEEE Trans. Electron Devices*, 2022, **69**(2), 622–630, DOI: [10.1109/TED.2021.3138375](https://doi.org/10.1109/TED.2021.3138375).
- 74 S. Bai, X. Guo, T. Chen, Y. Zhang and H. Yang, Solution Process Fabrication of Silver Nanowire Composite Transparent Conductive Films with Tunable Work Function, *Thin Solid Films*, 2020, **709**(May), 138096, DOI: [10.1016/j.tsf.2020.138096](https://doi.org/10.1016/j.tsf.2020.138096).
- 75 L. Barraud, Z. C. Holman, N. Badel, P. Reiss, A. Descoedres, C. Battaglia, S. De Wolf and C. Ballif, Hydrogen-Doped Indium Oxide/Indium Tin Oxide Bilayers for High-Efficiency Silicon Heterojunction Solar Cells, *Sol. Energy Mater. Sol. Cells*, 2013, **115**, 151–156, DOI: [10.1016/j.solmat.2013.03.024](https://doi.org/10.1016/j.solmat.2013.03.024).
- 76 P. Fooladvand, M. Eskandari, D. Fathi and N. Das, Single-Walled Carbon Nanotube as Hole Transport Layer in Perovskite Solar Cell: Efficiency Enhancement, *Energy Rep.*,



- 2023, **10**(October), 3652–3664, DOI: [10.1016/j.egy.2023.10.020](https://doi.org/10.1016/j.egy.2023.10.020).
- 77 M. A. Islam, J. Al Rafi and M. A. Uddin, Modeling and Formation of a Single-Walled Carbon Nanotube (SWCNT) Based Heterostructure for Efficient Solar Energy: Performance and Defect Analysis by Numerical Simulation, *AIP Adv.*, 2023, **13**(11), 115201, DOI: [10.1063/5.0167228](https://doi.org/10.1063/5.0167228).
- 78 J. Nomoto, I. Yamaguchi, T. Nakajima, Y. Matsubayashi and T. Tsuchiya, Excimer Laser Annealing Method for Achieving Low Electrical Resistivity and High Work Function in Transparent Conductive Amorphous In<sub>2</sub>O<sub>3</sub>:Zn Films on a Polyethylene Terephthalate Substrate, *Thin Solid Films*, 2020, **698**(January), 137867, DOI: [10.1016/j.tsf.2020.137867](https://doi.org/10.1016/j.tsf.2020.137867).
- 79 B. Bissig, R. Carron, L. Greuter, S. Nishiwaki, E. Avancini, C. Andres, T. Feurer, S. Buecheler and A. N. Tiwari, Novel Back Contact Reflector for High Efficiency and Double-Graded Cu(In,Ga)Se<sub>2</sub> Thin-Film Solar Cells, *Prog. Photovoltaics Res. Appl.*, 2018, **26**(11), 894–900, DOI: [10.1002/pip.3029](https://doi.org/10.1002/pip.3029).
- 80 F. Behrouznejad, S. Shahbazi, N. Taghavinia, H. P. Wu and E. Wei-Guang Diau, A Study on Utilizing Different Metals as the Back Contact of CH<sub>3</sub>NH<sub>3</sub>PbI<sub>3</sub> Perovskite Solar Cells, *J. Mater. Chem. A*, 2016, **4**(35), 13488–13498, DOI: [10.1039/c6ta05938d](https://doi.org/10.1039/c6ta05938d).
- 81 L. Yang, T. Xu, Z. Bai and S. Qin, Improved Open-Circuit Voltage of AZO/CsPbBr<sub>3</sub>/Carbon Structure Perovskite Solar Cells by an Al-Doped ZnO Electron Transport Layer, *J. Phys. Chem. C*, 2023, **127**(15), 7492–7500, DOI: [10.1021/acs.jpcc.3c00080](https://doi.org/10.1021/acs.jpcc.3c00080).
- 82 T. Wahl, J. Hanisch, S. Meier, M. Schultes and E. Ahlswede, Sputtered Indium Zinc Oxide Rear Electrodes for Inverted Semitransparent Perovskite Solar Cells without Using a Protective Buffer Layer, *Org. Electron.*, 2018, **54**(December 2017), 48–53, DOI: [10.1016/j.orgel.2017.12.020](https://doi.org/10.1016/j.orgel.2017.12.020).
- 83 Q. Jiang, Z. Song, R. C. Bramante, P. F. Ndione, R. Tirawat, J. J. Berry, Y. Yan and K. Zhu, Highly Efficient Bifacial Single-Junction Perovskite Solar Cells, *Joule*, 2023, **7**(7), 1573–555, DOI: [10.1016/j.joule.2023.06.001](https://doi.org/10.1016/j.joule.2023.06.001).
- 84 W. Wang, R. Liu, C. Dong, Y. Xie, M. Jiang, G. Dong and H. Zhou, Wet-Chemical Surface Texturing of AZO Substrate for Improved Perovskite Solar Cells, *J. Alloys Compd.*, 2023, **963**(171105), 1–7, DOI: [10.1016/j.jallcom.2023.171105](https://doi.org/10.1016/j.jallcom.2023.171105).
- 85 S. Pang, X. Li, H. Dong, D. Chen, W. Zhu, J. Chang, Z. Lin, H. Xi, J. Zhang, C. Zhang and Y. Hao, Efficient Bifacial Semitransparent Perovskite Solar Cells Using Ag/V<sub>2</sub>O<sub>5</sub> as Transparent Anodes, *ACS Appl. Mater. Interfaces*, 2018, **10**(15), 12731–12739, DOI: [10.1021/acsami.8b01611](https://doi.org/10.1021/acsami.8b01611).

